Available online at www.sciencedirect.com
ScienceDirect
Trans. Nonferrous Met. Soc. China 31(2021) 2871−2884
Transactions of Nonferrous Metals Society of China
www.tnmsc.cn

Numerical simulation of powder effect on solidification in directed energy deposition additive manufacturing

Xin-xin YAO, Jian-yu LI, Yi-fei WANG, Xiang GAO, Zhao ZHANG

State Key Laboratory of Structural Analysis for Industrial Equipment, Department of Engineering Mechanics, Faculty of Vehicle Engineering and Mechanics, Dalian University of Technology, Dalian 116024, China

Received 12 October 2020; accepted 20 April 2021

Abstract: An integrated simulation of powder effects on particle temperature and microstructural evolution in laser directed energy deposition additive manufacturing process was carried out. The spatial distribution of the flying powder particles was simulated by the discrete element method to calculate the energy for the flying powder particles under the laser−particle interaction with electromagnetic wave analysis. Combined with the phase field method, the influence of particle size on the microstructural evolution was studied. The microstructural evolution is validated through comparison with experimental observation. Results indicate that the narrow particle size distribution is beneficial to obtaining a more uniform temperature distribution on the deposited layers and forming smaller equiaxed grains near the side surfaces of the sample. Appropriate powder particle size is beneficial to the conversion of the electromagnetic energy into heat. Particles with small size are recommended to form equiaxed grains and to improve product quality. Appropriate powder flow rate improves the laser energy efficiency, and higher powder flow rate leads to more uniform equiaxed grains on both sides of the cross-section.

Key words: additive manufacturing; powder particle; phase field; microstructural evolution; particle size distribution

1 Introduction

Additive manufacturing (AM) is now quickly developed and applied to industries for its advantages on design freedom and manufacturing flexibility [1−3]. Directed energy deposition additive manufacturing (DEDAM) is a relatively mature additive manufacturing technology and has been applied in many fields such as biomedical industries, aerospace application and fine parts processing [4]. Nonetheless, DEDAM faces many challenges including inadequate understanding of various observed defects, which include thermal distortion [5,6], cracking [7,8], surface quality [9], thermal residual stress [10,11], and high cost of the DEDAM equipment and raw materials [12]. A deep understanding of thermal variations is critical to predict the microstructural evolution and mechanical performance further in parts made by DEDAM [13].

During the DEMAM process, many factors, including the powder material, the powder particle size and the particle size distribution, the absorption of laser radiation and the powder flow-rate [14−17], need to be considered and designed. To optimize the DEDAM processing, numerical simulation is essential to understand DEDAM process which is different to the conventional experimental trial-and-error method [18]. GUSAROV et al [19] considered the effects of the radiation transfer and the thermal diffusion and built a theoretical model to calculate the temperature field. There is a relationship between the heat source and the absorptivity profile along the depth direction. MUKHERJEE et al [20] developed a volumetric heat source model with the

Corresponding author: Zhao ZHANG, Tel/Fax: +86-411-84708432, E-mail: zhangz@dlut.edu.cn
DOI: 10.1016/S1003-6326(21)65700-X

interactions between the laser and the flying metal powder particles. The preheating temperatures of the activated elements are then calculated by considering the energy density per unit area of laser power and surface area of powder particles. YIN et al [21] considered the effective thermal conductivity, the volumetric enthalpy and the absorptance change to build a volumetric heat source. In this model, the laser energy presented an exponential decay profile along the vertical direction and a Gaussian profile on the cross-section during the selective laser melting process. YAN et al [22] built a process−structure−properties prediction framework to predict the resultant mechanical properties from the given manufacturing process parameters and intrinsic material properties. LIU et al [23] employed a polycrystal phase field model to study the microstructural evolution during AM and the controlling of the grain structures and the textures. GE et al [24] used the Monte−Carlo model to simulate the microstructural evolution in the laser metal deposition AM of titanium alloy.

The existing models based on the heat resource and microstructural evolution provide detailed insight into DEDAM. However, the link between the powder quality (powder particle distribution, particle size and powder flow rate) and the microstructural evolution of DED AM product has not been studied. Therefore, it is necessary to establish a multiscale computational framework to investigate how the powder feature affects the thermal distribution and the microstructural evolution in DED. This is our motivation of current work. Discrete element method was used to simulate the flying of the powder particles from the nozzles to the substrate in the laser beam. Then, a coupled electromagnetic wave-heating method was used to calculate the consumed energy under the laser−particle interaction. The phase field method was finally adopted to investigate microstructural evolution in DEDAM.

2 Numerical models

2.1 Particle-generation model

Figure 1 shows the schematic of the interaction between the laser and the metal powder stream. When the particles fly from the nozzles along the direction of tubes and fall on the substrate after being irradiated by the laser, the laser energy can be reduced in its intensity distribution [25]. In order to consider the laser−particle interaction, some assumptions are made: (1) the shape of metal particles is set to be spherical; (2) the distribution of particle size is uniform; (3) the initial velocity is the same for all the particles. Based on the above assumptions, a series of spatially distributed powder particles are generated based on the discrete element method (DEM). The movement of the individual particle is described by its translational and rotational motions [26]:

$$m_i \frac{\mathrm{d}\boldsymbol{v}_i}{\mathrm{d}t} = \sum_j (\boldsymbol{F}_{\mathrm{n},ij} + \boldsymbol{F}_{\mathrm{s},ij}) + m_i \boldsymbol{g} \tag{1}$$

$$I_i \frac{\mathrm{d}\boldsymbol{\omega}_i}{\mathrm{d}t} = \sum_j (\boldsymbol{R}_i \times \boldsymbol{F}_{\mathrm{s},ij} - \mu_\mathrm{r} R_i |\boldsymbol{F}_{\mathrm{n},ij}| \frac{\boldsymbol{\omega}_i}{|\boldsymbol{\omega}_i|}) \tag{2}$$

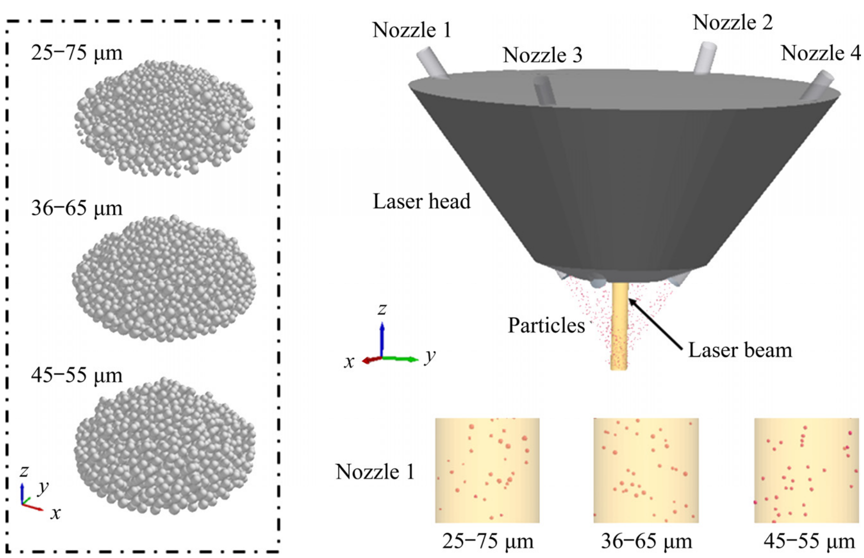

Fig. 1 Schematic showing interaction between laser beam and powder stream

where m_i, $\boldsymbol{g}$, I_i, $\boldsymbol{v}_i$, and $\boldsymbol{\omega}_i$ are the mass, gravitational acceleration, moment of inertia, translational velocity, and angular velocity, respectively; $\boldsymbol{F}_{n,ij}$ is the normal contact force and $\boldsymbol{F}_{s,ij}$ is the tangential contact force; $\boldsymbol{R}_i$ is a vector from the center of the particle to the contact point with a magnitude equal to the particle radius R_i; μ_r is the rolling friction coefficient. The velocity of the flying particles is 2 m/s. Detailed parameters about the particle−generation model can be found in our previous work [27].

2.2 Electromagnetic heating model

The laser beam is treated as an electromagnetic wave with a high frequency essentially. The laser power (P) can be written as

$$P=\frac{1}{\mu}\int \boldsymbol{E}\times\boldsymbol{B}\mathrm{d}A \tag{3}$$

where μ is the permeability; $\boldsymbol{E}$ is the electric field intensity vector; $\boldsymbol{B}$ is the magnetic induction intensity vector; A is the cross-section area of the laser.

The Maxwell's equations in the electromagnetic analysis can be expressed in the differential form [28]:

$$\nabla\boldsymbol{B}=0 \tag{4}$$

$$\frac{\partial\boldsymbol{B}}{\partial t}=-\nabla\times\boldsymbol{E} \tag{5}$$

$$\nabla\cdot\boldsymbol{D}=\gamma \tag{6}$$

$$\frac{\partial\boldsymbol{D}}{\partial t}=\nabla\times\boldsymbol{H}-\boldsymbol{J} \tag{7}$$

where γ is the free-charge density; $\boldsymbol{D}$ is the electric displacement vector; $\boldsymbol{H}$ is the magnetic field intensity vector, $\boldsymbol{P}$ is the polarization density vector of particles, and $\boldsymbol{J}$ is the conduction current density vector in media. Detailed parameters can be found in our previous work [27]. To solve the electromagnetic field distributions, the above equations are combined as

$$\nabla\times\left(\nabla\times\boldsymbol{E}\right)=-\mu_0\sigma\frac{\partial\boldsymbol{E}}{\partial t}-\mu_0\varepsilon_0\frac{\partial^2\boldsymbol{E}}{\partial t^2}-\mu_0\frac{\partial^2\boldsymbol{P}}{\partial t^2} \tag{8}$$

where μ_0 is the vacuum permeability; σ is the electric conductivity of particle; ε_0 is the vacuum permittivity.

The power density (q_{total}) consumed by the flying powder particles can be expressed as [29]

$$q_{\text{total}}=\frac{1}{2}\mathrm{Re}(\boldsymbol{J}\cdot\boldsymbol{E})+\frac{1}{2}\mathrm{Re}(\mathrm{i}\omega\boldsymbol{B}\cdot\boldsymbol{H}) \tag{9}$$

The heat conduction for particles and the boundary condition on the surface of components can be expressed as [30,31]

$$\rho(T)c(T)\frac{\partial T}{\partial t}+q_{\text{total}}=\nabla\cdot[k(T)\nabla T] \tag{10}$$

$$k(T)\nabla\cdot T=h(T_\mathrm{a}-T)+\varepsilon_R\sigma_R(T_\mathrm{a}^{\,4}-T^4) \tag{11}$$

where T is the temperature, $\rho(T)$ is the density, $c(T)$ is the specific heat capacity, $k(T)$ is the thermal conductivity, ε_R(=0.4) is the emissivity, σ_R is the Stefan-Boltzmann constant, T_a(=293.15 K) is the ambient temperature, and h(=100 W/(m^2·K)) is the convective heat coefficient [32]. In this model, the phase change of particles (solid to liquid) is not considered during the flight process due to short flight time. Powder particles from one nozzle are selected, as depicted in Fig. 2.

2.3 Finite element heat transfer model

Finite element method (FEM) for the thermal transfer is adopted to calculate the spatial and

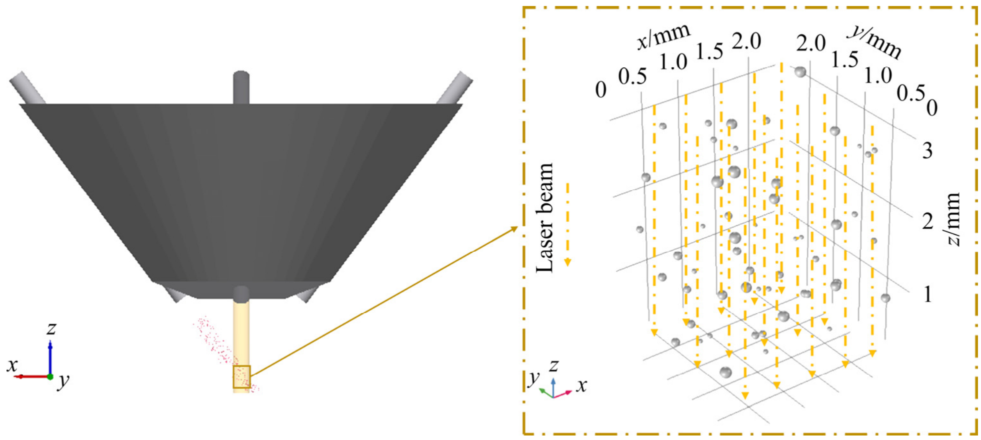

Fig. 2 Schematic of electromagnetic laser heating model

temporal temperatures. The governing energy equation accompanying with the volumetric heat flux is expressed as

$$\rho(T)c(T)\frac{\partial T}{\partial t}+Q_{\mathrm{de}}=\nabla\cdot[k(T)\nabla T] \tag{12}$$

where Q_{de} denotes the body heat flux. The same boundary condition as Eq. (11) is applied on the component surface. h=30 W/(m^2·K) is selected in the FEM model. The preheating temperature is 293.15 K for the substrate. The volume−average temperature can be calculated by the electro-magnetic heating transfer model for deposit.

The improved double-ellipsoid heat source can be written as

$$Q_{\mathrm{de}}(x,y,z,t)=\begin{cases} P\dfrac{6\sqrt{3}\eta_{\mathrm{s}}\eta_{\mathrm{power}}f_{\mathrm{f}}}{a_{\mathrm{f}}bc\pi\sqrt{\pi}}\cdot \\ \quad \exp\left\{-3\left[\left(\dfrac{x+vt}{a_{\mathrm{f}}}\right)^2+\left(\dfrac{y}{b}\right)^2+\left(\dfrac{z}{c}\right)^2\right]\right\}, \\ \quad x,y,z\in \text{front part} \\ P\dfrac{6\sqrt{3}\eta_{\mathrm{s}}\eta_{\mathrm{power}}f_{\mathrm{r}}}{a_{\mathrm{r}}bc\pi\sqrt{\pi}}\cdot \\ \quad \exp\left\{-3\left[\left(\dfrac{x+vt}{a_{\mathrm{r}}}\right)^2+\left(\dfrac{y}{b}\right)^2+\left(\dfrac{z}{c}\right)^2\right]\right\}, \\ \quad x,y,z\in \text{rear part} \end{cases} \tag{13}$$

where a_{f}, a_{r}, b and c are constants which satisfy a_{f}=c, a_{r}=2c, b=1.5 mm and c=1 mm [33]; f_{f} and f_{r} are the heat-input coefficients; η_{s} is the absorption coefficient; η_{power} is the heat-transfer reduction coefficient of laser energy due to the laser−particle interaction; t is the time. The temperature-dependent material properties and detailed parameters can be obtained in our previous work [27].

2.4 Phase field model for grain growth

The polycrystal phase-field method (PFM) established by KRILL and CHEN [34] is employed to simulate the grain growth during the laser additive manufacturing. PFM is a powerful tool to effectively simulate the complex microstructural evolution during solidification [35−40]. In PFM, a series of continuous field variables are adopted to represent the microstructure and the reduction of the total free energy is the driving force. The total free energy $F(t)$ can be expressed as

$$F(t)=\int[f_0(\eta_1(\boldsymbol{r},\ t),\ \eta_2(\boldsymbol{r},\ t),\ \cdots,\ \eta_Q(\boldsymbol{r},\ t))+ \sum_{q=1}^{Q}\frac{k_q}{2}(\nabla\eta_q(\boldsymbol{r},\ t))^2]\mathrm{d}\boldsymbol{r} \tag{14}$$

where f_0 represents the local free energy density; $\boldsymbol{r}$ is the position vector; k_q is the gradient energy coefficient related to the grain boundary energies; $\{\eta_q\}$ represents the crystallographic orientation of each grain. The local free energy density is given as

$$f_0(\{\eta_q(\boldsymbol{r},\ t)\})=-\frac{a}{2}\sum_{q=1}^{Q}\eta_q^2(\boldsymbol{r},\ t)+\frac{b}{4}(\sum_{q=1}^{Q}\eta_q^2(\boldsymbol{r},\ t))^2+ (c-\frac{b}{2})\sum_{q=1}^{Q}\sum_{s>q}^{Q}\eta_q^2(\boldsymbol{r},\ t)\eta_s^2(\boldsymbol{r},\ t) \tag{15}$$

where a, b and c are constants that satisfy a=b and c>a/2.

Allen−Cahn equation is adopted to solve the order parameters η_q and expressed as

$$\frac{\partial\eta_q(\boldsymbol{r},t)}{\partial t}=-L_q(T)\frac{\delta F(t)}{\delta\eta_q(\boldsymbol{r},\ t)}\quad (q=1,\ 2,\ \cdots,\ Q) \tag{16}$$

where L_q denotes the grain boundary mobility. To describe the effect of temperature on the grain boundary mobility, the modified Arrhenius type equation is used as follows [41]:

$$L_q(T)=L_0\left(\frac{T}{T_{\mathrm{a}}}\right)^m\exp\left(-\frac{\Delta Q}{R_{\mathrm{g}}T}\right) \tag{17}$$

where L_0 and m are constants; ΔQ(=97 kJ/mol) is the activation energy for grain growth [42]; R_{g}(=8.314 J/(mol·K)) is the mole gas constant. Forward difference method is used to solve Eq. (16) and zero-flux boundary condition is applied to all the boundaries according to Ref. [23]. Temperatures of all lattice points in PFM can be obtained by the linear interpolation of the points extracted from FEM and the details can be found in our previous work [27].

3 Experimental validation

To validate the proposed thermal model, the melt pool size in the numerical model is compared with the experimental observation, as shown in Fig. 3. The used machine for DEDAM was previously introduced in Refs. [6,14,27]. In the

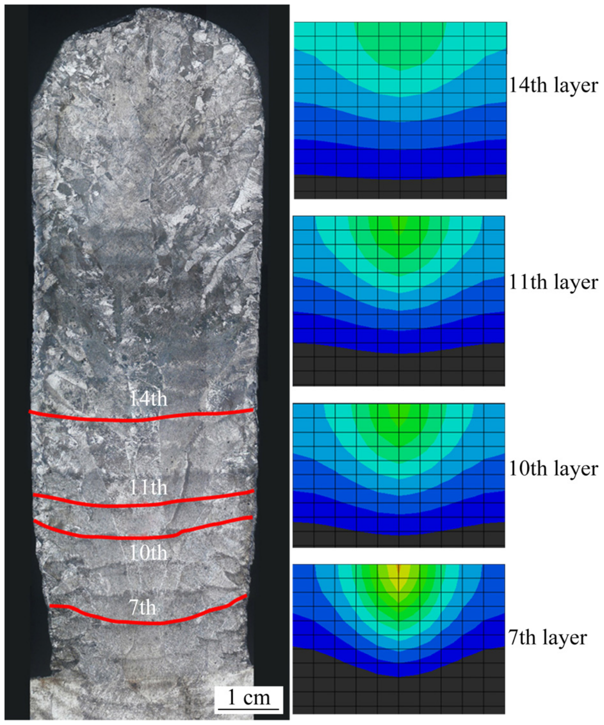

Fig. 3 Comparison of melt pool sizes between experiment (a) and numerical model (b)

current experiment, the powder size ranges from 60 to 110 μm. The laser power is 1000 W. The radius of the laser beam is 1.5 mm. The powder flow rate is 9.15 g/min. The experimental settings are selected to be the same with the numerical model for accurate comparison. With the increase of the build height, the border of the melt pool becomes flatter. The comparison shows the validity of the used thermal model.

4 Results and discussion

4.1 Effect of powder particle distribution

The microstructural evolution can be affected by the particle size distribution [43]. To study the effect of the powder particle size distribution, three kinds of particle distributions (radii within 25−75, 35−65 and 45−55 μm) with the same average radius of 50 μm are built. Figure 4 depicts the temperature of particles with different radii. It is found that the temperatures of the particles decrease with the increase of the particle radius, which is similar to the cases in the microwave-heating problem [44]. When the particle radius ranges from 25 to 75 μm, the maximum temperature is 2491.2 K for the particle with smaller radius of 26.8 μm, while the minimum temperature is 398.5 K for the particle with larger radius of 69.3 μm. The average temperature of all the particles is 617.5 K. When the particle radius ranges from 35 to 65 μm, the maximum temperature is 1270.1 K for the particle with a radius of 37.84 μm, while the minimum temperature is 434.64 K for the particle with a radius of 63.30 μm. The temperature difference is 835.46 K and the average temperature is 655.6 K. When the particle radius ranges from 45 to 55 μm, the maximum temperature is 1024.9 K for the particle with a radius of 47.6 μm while the minimum temperature is 437.9 K for the particle with a radius of 52.14 μm. The temperature difference is 587 K and the average temperature is 703.8 K. Under the condition that the average radius keeps the same, larger variation in particle sizes leads to lower average temperature. Besides, higher temperature difference leads to both the overheating to smaller powder particles and insufficient heating to larger powder particles.

Figure 5 depicts the consumed laser power of particles with different radii. It is found that the laser energy absorbed by each particle is in random distribution with fluctuation. This fluctuation is related to the spatial distribution of particles in the electromagnetic field. For smaller particles, higher ratio of the metal skin depth to the particle radius leads to stronger power density and more efficient conversion of electromagnetic energy into heat.

The changes of the temperature and the consumed laser power density with radius are shown in Fig. 6. Similar to the consumed laser power density, the temperature is decreased with the increase of particle radius with fluctuations. To illustrate the effect of the spatial distribution on the consumed laser power, P_1 and P_2 with similar radii are selected for comparison. The radii are 29.82 and 29.76 μm for P_1 and P_2, as shown in Fig. 4(a). P_1 is located at the upper middle of the laser−particle interaction zone. The distribution of power loss density on the surface is more evenly distributed, which is beneficial to the energy absorption of particles. The maximum power density is 1.46×10^{15} W/m^3. P_2 is located at the bottom of the laser−particle interaction zone. The distribution of the power loss density is concentrated, which means lower energy absorption by particles. As the laser travels in the laser−particle interaction zone from top to bottom, the laser power is attenuated.

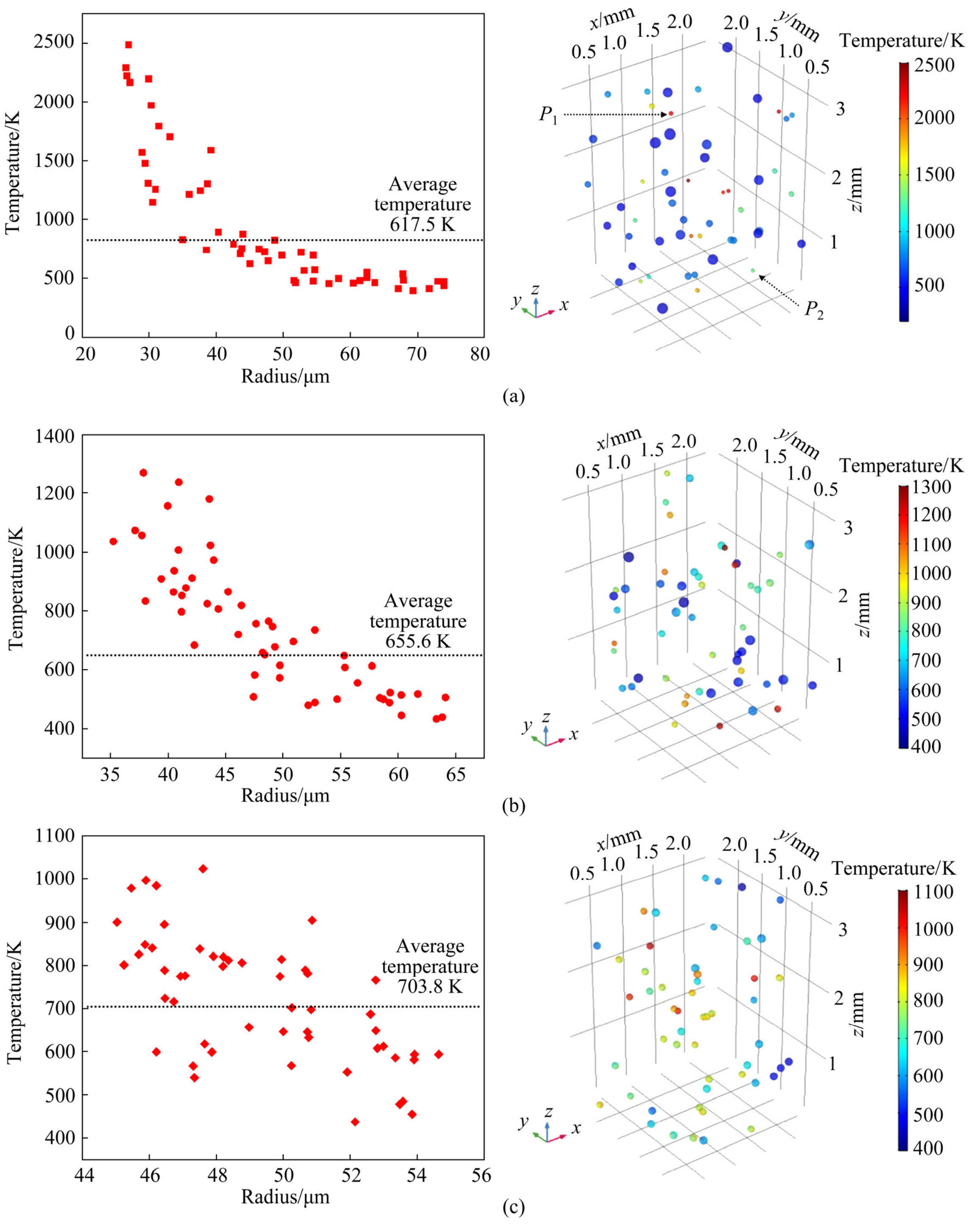

Fig. 4 Temperatures of particles with different particle size distributions: (a) Radius 25−75 μm; (b) Radius 35−65 μm; (c) Radius 45−55 μm

The maximum power density is 4.66×10^{14} W/m^3. The consumed laser power is 0.81 and 0.40 W for P_1 and P_2, respectively.

Figure 7 shows the average consumed laser power and the reduction rate of laser power. The average consumed powers are 0.62, 0.63 and 0.70 W for the particle radius distributions of 25−75, 35−65 and 45−55 μm, respectively. The reduction rates of laser power are 13.1%, 13.4% and 14.4% for the different particle radius distributions. As a result, the heat-transfer reduction coefficients of laser energy η_{power} applied in FEM are 0.869, 0.866 and 0.856 for those three particle radius distributions, respectively.

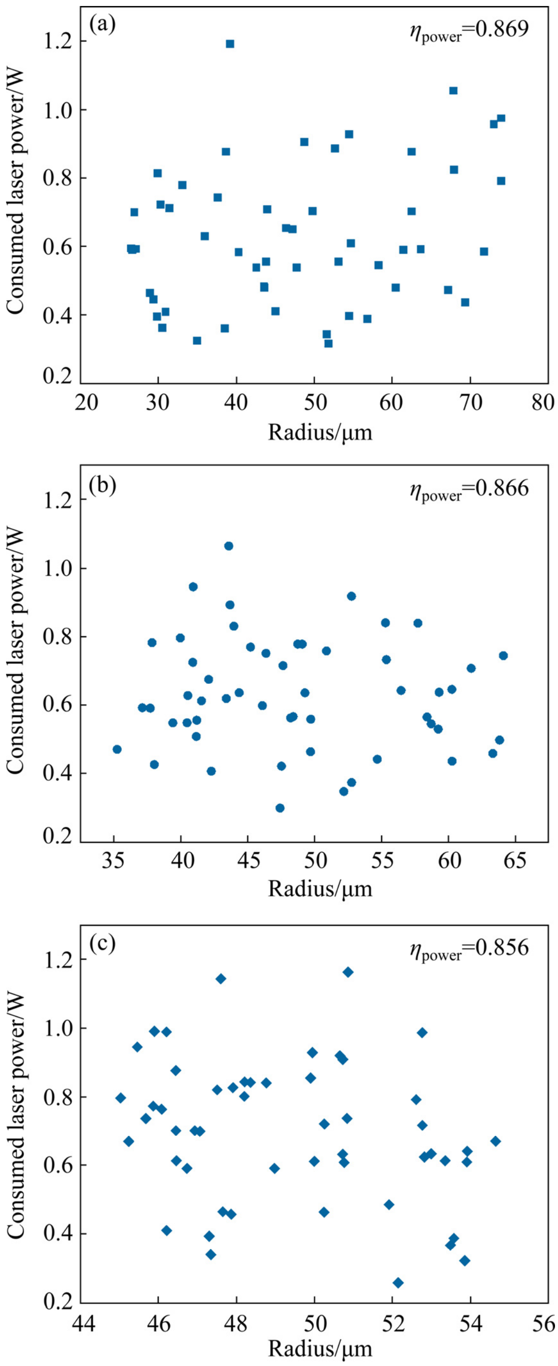

Fig. 5 Consumed laser powers of particles with different particle size distributions: (a) Radius 25−75 μm; (b) Radius 35−65 μm; (c) Radius 45−55 μm

Larger variation in particle radius distribution leads to less energy reduction consumed by laser-particle interaction.

Paths are selected in Fig. 8 to evaluate the effect of particle size distribution on the temperature histories in different cases. When the 10th deposited layer is scanned, the temperature varies from 1902.2 to 2012.5 K for particle radius distribution ranging from 25 to 75 μm. For particle radius distribution ranging from 35 to 65 μm, the temperature varies from 1900.1 to 2010.3 K. For particle radius distribution ranging from 45 to 55 μm, the temperature varies from 1894.8 to 2002.6 K. When the 15th deposited layer is scanned, the temperature varies from 1912.4 to 1935.7 K and 1911.2 to 1934.0 K, 1908.3 to 1925.1 K, respectively. Wider size distribution leads to more laser energy absorption on specimen which leads to higher temperature.

From the perspective of temperature gradient, the difference between different particle size distributions is further studied. As shown in Fig. 9, the temperature gradients along the vertical direction around the melt pools with different particle size distributions are compared. The maximum temperature gradients in the 10th layer are 3.53×10^5, 3.52×10^5 and 3.48×10^5 K/m for the radius distributions of 25−75, 35−65 and 45−55 μm, respectively. The minimum temperature gradients are 2.125×10^5, 2.123×10^5 and 2.075×10^5 K/m, respectively. The maximum temperature gradients in the 15th layer are 2.026×10^5, 2.012×10^5 and 1.911×10^5 K/m and the minimum temperature gradients are 1.768×10^5, 1.760×10^5 and 1.722×10^5 K/m, respectively. The wider size distribution leads to higher temperature gradient which decreases the nucleation rate.

The effect of the particle size distribution on the microstructural evolution is considered based on the previous results. The solidification behavior can be affected by two main variables, i.e., the temperature gradient (G) and the solidification velocity (v). The grain size is influenced by $G\times v$ while the columnar to equiaxed transition of grain structures is determined by G/v [31]. Related discussions are reported in our previous work [27]. Figure 10 shows microstructural morphologies with different particle size distributions obtained by phase-field simulation. β-grain is finally formed in the internal domain of the cross-section, as shown in Region A in Fig. 10(a). Lower temperature gradient is beneficial to the nucleation and the formation of the equiaxed grains. The detailed values of grain sizes are listed in Table 1. The average sizes of the equiaxed grains are 0.242, 0.233 and 0.231 mm and the average widths of β-grains are 0.53, 0.645 and 0.616 mm for particle

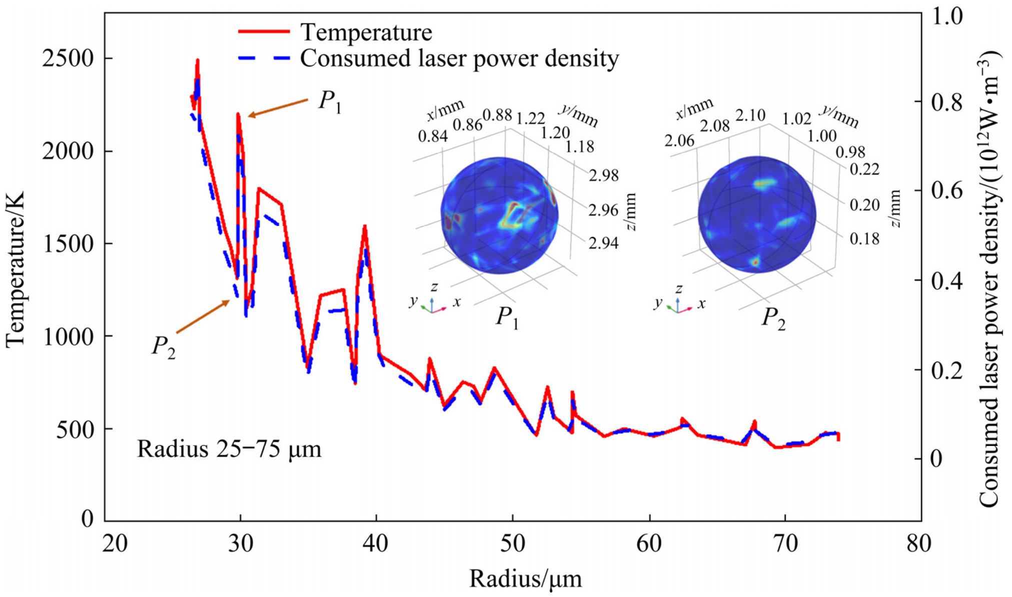

Fig. 6 Relationship between temperature and consumed laser power density

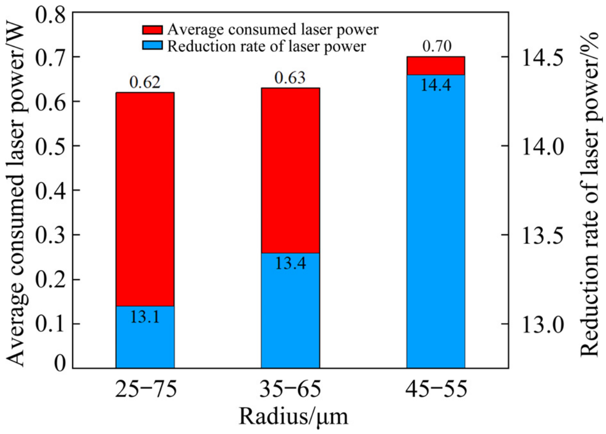

Fig. 7 Average consumed laser power and reduction rate

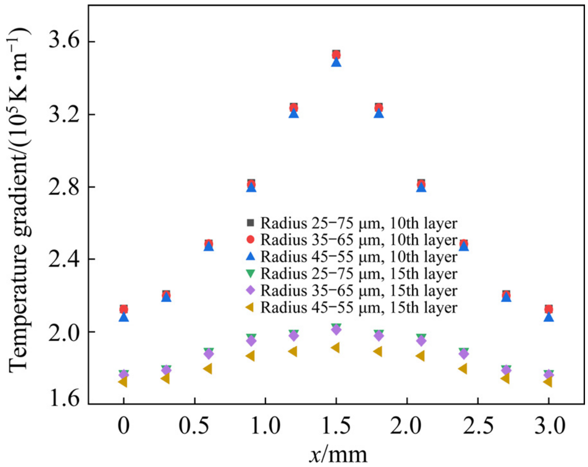

Fig. 9 Temperature gradient along vertical direction around melt pool with different particle size distributions

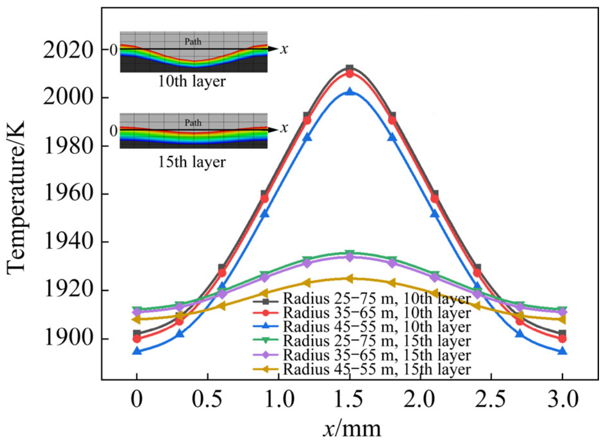

Fig. 8 Temperature distributions of selected paths with different particle size distributions (x is the distance to the left)

radius distributions of 25−75, 35−65 and 45−55 μm, respectively. Based on the above analysis, narrow distribution is suggested for more uniform temperature and for lower overheating which are beneficial to the improvement of the product quality.

4.2 Effect of powder particle size

Two electromagnetic wave−heat transfer models with the particles radii of 50 and 75 μm are built, as shown in Fig. 11. The powder flow rate is 9.15 g/min. The temperatures are 682.0 and 490.7 K, and the average consumed laser powers of particles are 0.66 and 1.11 W for particle sizes of 50

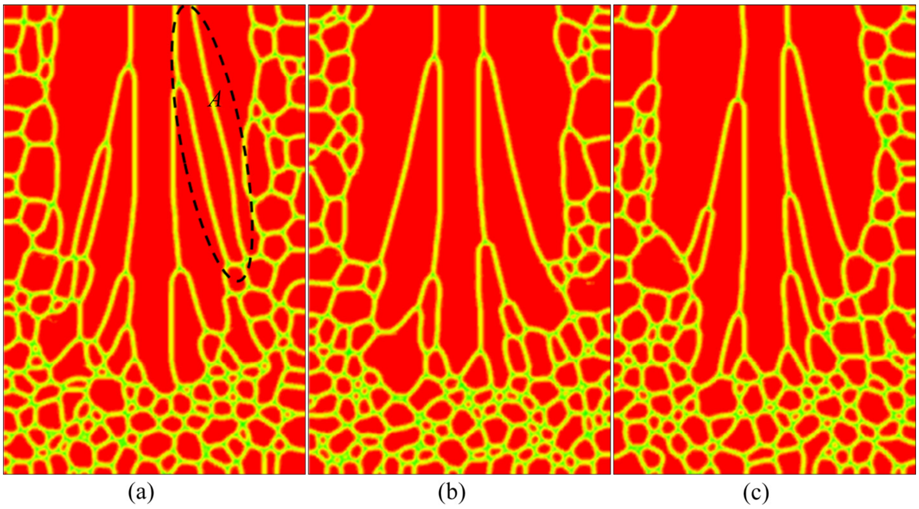

Fig. 10 Microstructural morphologies with different particle radius distributions obtained by phase-field simulation: (a) Radius 25−75 μm; (b) Radius 35−65 μm; (c) Radius 45−55 μm

Table 1 Comparison of grain sizes with different particle radius distributions

Particle radius/μm	Equiaxed grain size/mm	Width of β-grain/mm
25−75	0.242	0.53
35−65	0.233	0.645
45−55	0.231	0.616

and 75 μm, respectively. The larger particle absorbs more laser power with lower temperature. This phenomenon is also observed in Ref. [44]. Higher ratio of metal skin depth to particle radius leads to higher efficiency of the conversion from the electromagnetic energy to heat. The heat-transfer reduction coefficients for the particle radii of 50 and 75 μm are 0.8576 and 0.916, respectively. Thus, larger particles lead to higher heat-transfer reduction coefficient of laser energy, which causes higher temperatures.

The temperatures in different deposited layers are compared in Fig. 12. It is found that the temperature in the case with a particle radius of 75 μm is higher than that in the case with a particle radius of 50 μm. When the particle radius is 50 μm, the depths of the melt pool are 1.725 and 2.11 mm in the 10th and 15th layers, respectively. When the particle radius is 75 μm, the depths of the melt pool in the 10th and 15th layers are 1.850 and 2.335 mm, respectively.

The effect of the particle size on the temperature gradient along the vertical direction

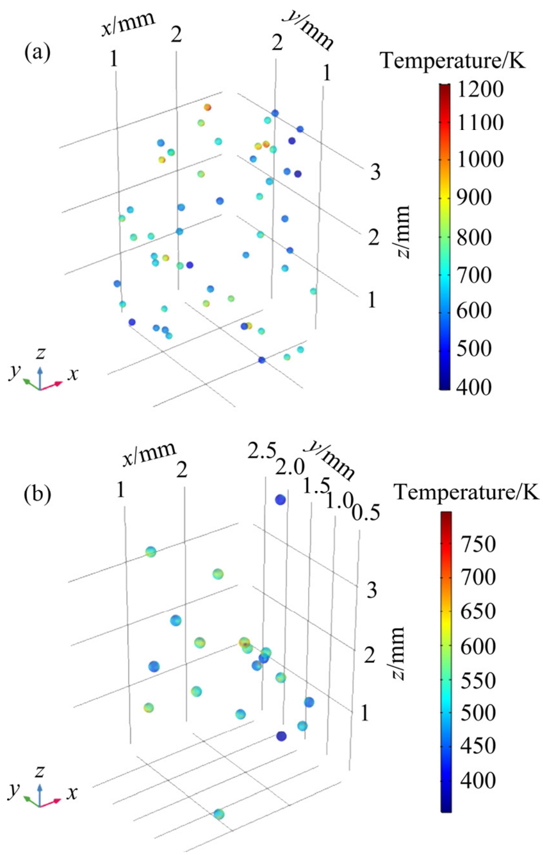

Fig. 11 Comparison of temperatures of particles with different particle radii: (a) 50 μm; (b) 75 μm

around the melt pool is shown in Fig. 13. It is found that the temperature gradient in the case of 75 μm particle radius is higher than that in the case of 50 μm in the external region (x<0.5 mm and x>2.5 mm). The temperature gradient in the case of 75 μm particle radius is lower than that in the case

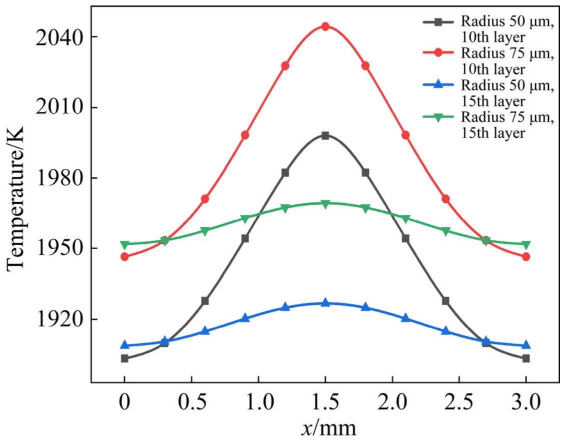

Fig. 12 Temperature distributions in deposited layers with different particle sizes

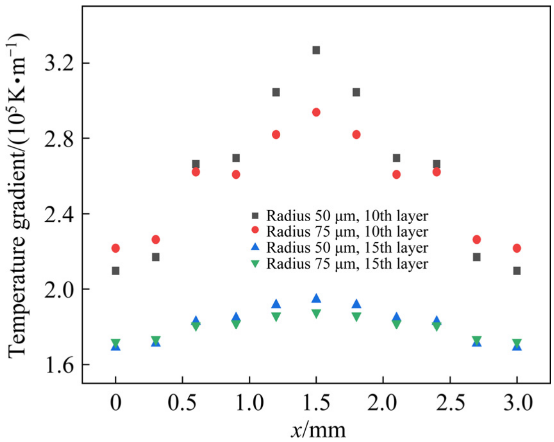

Fig. 13 Temperature gradient along vertical direction around melt pool with different particle sizes

of 50 μm in the internal region (0.5 mm<x<2.5 mm) of 10th layer. The temperature gradients at x=0 and x=0.3 mm are 2.217×10^5 and 2.263×10^5 K/m, respectively in the case of 75 μm particle radius. When the particle radius is decreased to 50 μm, the temperature gradients at x=0 and x=0.3 mm are changed to be 2.097×10^5 and 2.170×10^5 K/m, respectively.

Figure 14 shows microstructural morphologies in the deposited layers with different particle sizes obtained by phase-field simulation. The comparison of Regions *B* and *C* shows that higher temperature gradient is not beneficial to forming equiaxed grains. This phenomenon is consistent with Ref. [45]. Besides, more β-grains are found in Region *D* for the case with particle radius of 75 μm. The average sizes of the equiaxed grains are 0.262 and 0.244 mm and the average widths of β-grain are 0.625 and 0.563 mm for particle sizes of 50 and 75 μm, respectively. Based on the above analysis, particles with smaller sizes are recommended to form equiaxed grains and to improve product quality.

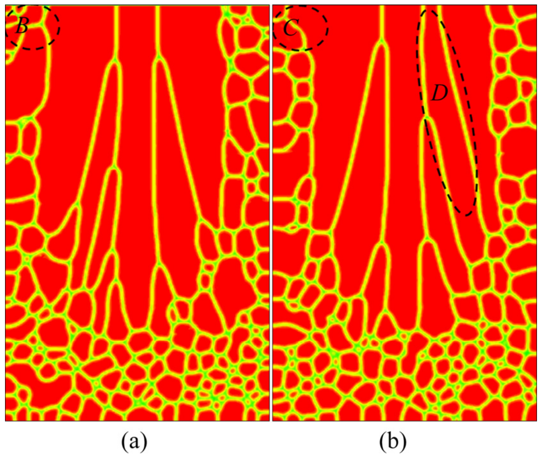

Fig. 14 Microstructural morphologies with different particles radii obtained by phase-field simulation: (a) 50 μm; (b) 75 μm

4.3 Effect of powder flow rate

The powder flow rate is also one of the variables that affect the reduction of laser power and the temperature distribution in the DED process. When the powder flow rate increases from 9.15 to 15 g/min, the number of particles increases from 53 to 87 accordingly. The electromagnetic wave−heat transfer model based on the particle radius distribution of 45−55 μm is built. The temperature and the consumed power of particles are shown in Fig. 15. Compared with the case in which the powder flow rate is 9.15 g/min, the average temperature at the powder flow rate of 15 g/min decreases to 643.7 K and the consumed laser power decreases to 0.62 W, which is caused by the covering of particles as a result of increased particles in the limited region [46]. Meanwhile, more particles consume higher laser power, which leads to the decrease of the heat-transfer reduction coefficient to 0.7842. Higher powder flow rate is suggested to avoid the inefficient laser−particle interaction and the excessive laser energy loss.

Because of the increase of the powder flow rate, the thickness of the single deposited layer increases from 0.3 to 0.4 mm. The effect of the powder flow rate on the size of the melt pool is shown in Fig. 16. When the flow rate is 9.15 g/min, the maximum temperature is 2644 K and the depths

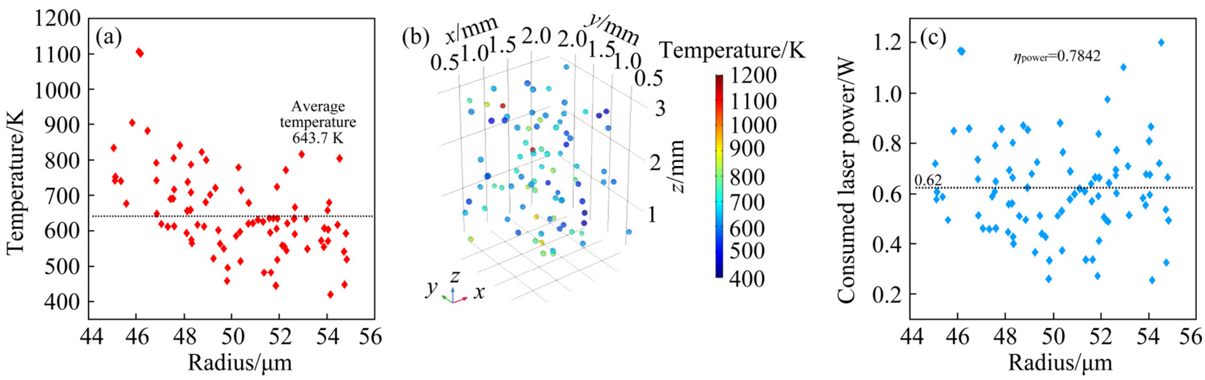

Fig. 15 Simulation results with powder flow rate of 15 g/min: (a) Change of temperature with particle radius; (b) Temperature contour; (c) Change of consumed laser power with particle radius

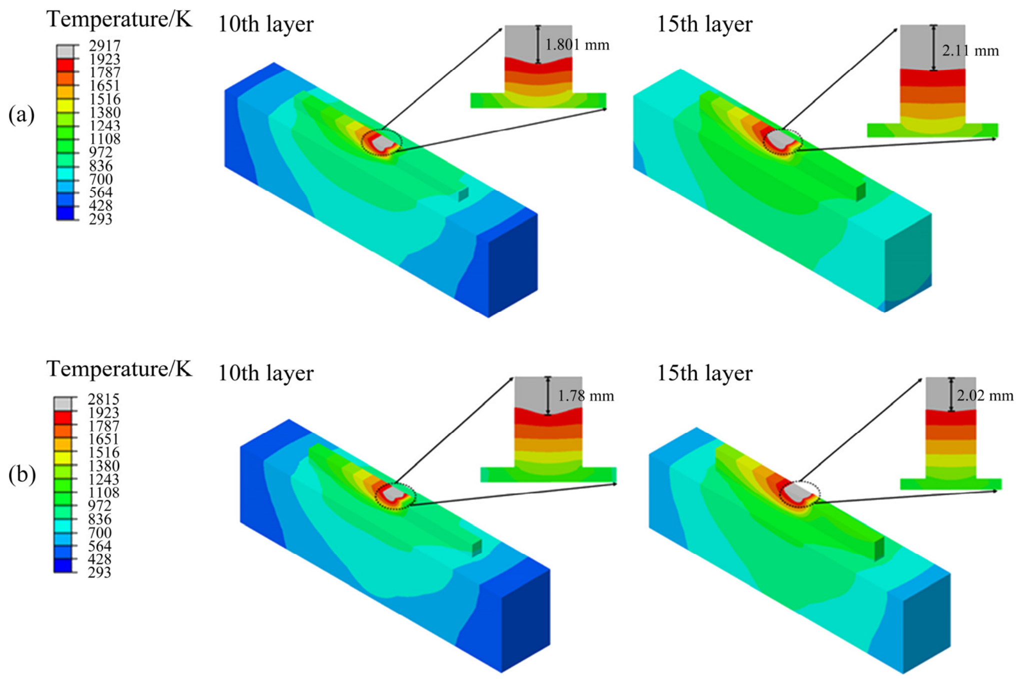

Fig. 16 Effect of powder flow rate on size of melt pool in different deposited layers: (a) Powder flow rate of 9.15 g/min and single layer thickness of 0.3 mm; (b) Powder flow rate of 15 g/min and single layer thickness of 0.4 mm

of the melt pool of the 10th and 15th layers are 1.801 and 2.11 mm, respectively. As the powder flow rate increases to 15 g/min, the depths of the melt pool of the 10th and 15th layers decrease to 1.78 and 2.02 mm, respectively.

Due to the increase of the deposited layer thickness, the re-melting portion in the former deposited layer is decreased. Figure 17 shows the microstructural morphology with the powder flow rate of 15 g/min obtained by phase-field simulation. It is observed that the growth of the equiaxed grains on both sides of the cross- section is more uniform and bigger due to the decrease of the re-melting portion caused by the increased deposited layer thickness.

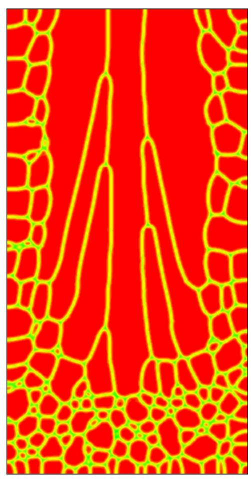

Fig. 17 Microstructural morphology with powder flow rate of 15 g/min obtained by phase-field simulation

5 Conclusions

(1) Narrower particle size distribution is suggested for more uniform temperature distribution on the deposited layers and to form smaller equiaxed grain near the two side surfaces of DED specimen.

(2) Larger variation in particle sizes leads to lower average temperature on the deposited layers due to the laser−particle interaction in the laser beam.

(3) Proper powder particle size is beneficial to the conversion of the electromagnetic energy into heat.

(4) Particles with small sizes are recommended to form equiaxed grains.

(5) Appropriate powder flow rate can improve the efficiency of laser. Larger powder flow rate leads to more uniform and bigger equiaxed grains on both sides of the cross-section.

Acknowledgments

The authors are grateful for the financial supports from the National Natural Science Foundation of China (No. 11572074), and the Liaoning Provincial Natural Science Foundation, China (No. 2019-KF-05-07)

References

[1] MARTIN J H, YAHATA B D, HUNDLEY J M, MAYER J A, SCHAEDLER T A, POLLOCK T M. 3D printing of high-strength aluminium alloys [J]. Nature, 2017, 549: 365−369.

[2] WANG Pei, ECKERT J, PRASHANTH K, WU Ming-wei, KABAN I, XI Li-xia, SCUDINO S. A review of particulate-reinforced aluminum matrix composites fabricated by selective laser melting [J]. Transactions of Nonferrous Metals Society of China, 2020, 30: 2001−2034.

[3] HAN Li-ying, WANG Cun-shan. Microstructure and properties of $Ti_{64.51}Fe_{26.40}Zr_{5.86}Sn_{2.93}Y_{0.30}$ biomedical alloy fabricated by laser additive manufacturing [J]. Transactions of Nonferrous Metals Society of China, 2020, 30: 3274−3286.

[4] BUSACHI A, ERKOYUNCU J, COLEGROVE P, MARTINA F, WATTS C, DRAKE R. A review of additive manufacturing technology and cost estimation techniques for the defence sector [J]. CIRP Journal of Manufacturing Science and Technology, 2017, 19: 117−128.

[5] LINDGREN L E, LUNDBÄCK A, FISK M, PEDERSON R, ANDERSSON J. Simulation of additive manufacturing using coupled constitutive and microstructure models [J]. Additive Manufacturing, 2016, 12: 144−158.

[6] ZHANG Zhao, GE Peng, YAO Xin-xin, LI Tao, LIU Wei-wei. Numerical studies of residual states and scaling effects in laser-directed energy deposition additive manufacturing [J]. International Journal of Advanced Manufacturing Technology, 2020, 108: 1233−1247.

[7] ZHAO Zhuang, CHEN Jing, TAN Hua, TANG Jin-gang, LIN Xin. In situ tailoring microstructure in laser solid formed titanium alloy for superior fatigue crack growth resistance [J]. Scripta Materialia, 2020, 174: 53−57.

[8] GLODEŽ S, KLEMENC J, ZUPANIČ F, VESENJAK M. High-cycle fatigue and fracture behaviours of SLM $AlSi_{10}Mg$ alloy [J]. Transactions of Nonferrous Metals Society of China, 2020, 30: 2577−2589.

[9] MACONACHIE T, LEARY M, LOZANOVSKI B, ZHANG Xue-zhe, QIAN Ma, FARUQUE O, BRANDT M. SLM lattice structures: Properties, performance, applications and challenges [J]. Materials & Design, 2019, 183: 108137.

[10] MOSER D, CULLINAN M, MURTHY J. Multi-scale computational modeling of residual stress in selective laser melting with uncertainty quantification [J]. Additive Manufacturing, 2019, 29: 100770.

[11] LINDGREN L E, EDBERG J, AKERSTROM P, ZHANG Z. Modeling of thermal stresses in low alloy steels [J]. Journal of Thermal Stresses, 2019, 42(6): 725−743.

[12] MISHRA A K, KUMAR A. Numerical and experimental analysis of the effect of volumetric energy absorption in powder layer on thermal-fluidic transport in selective laser melting of Ti6Al4V [J]. Optics & Laser Technology, 2019, 111: 227−239.

[13] PLOTKOWSKI A, KIRKA M M, BABU S S. Verification and validation of a rapid heat transfer calculation methodology for transient melt pool solidification conditions in powder bed metal additive manufacturing [J]. Additive Manufacturing, 2017, 18: 256−268.

[14] ZHANG Zhao, GE Peng, LI Tao, LINDGREN L E, LIU Wei-wei, ZHAO Guo-zhong, GUO Xu. Electromagnetic wave-based analysis of laser–particle interactions in directed energy deposition additive manufacturing [J]. Additive Manufacturing, 2020, 34: 101284.

[15] XIA Yang, DONG Zhao-wang, GUO Xue-yi, TIAN Qing-hua, LIU Yong. Towards a circular metal additive manufacturing through recycling of materials: A mini review [J]. Journal of Central South University, 2020, 27: 1134−1145.

[16] YANG Xin, REN Yao-jia, LIU Shi-feng, WANG Qing-juan, SHI Ming-jun. Microstructure and tensile property of SLM 316L stainless steel manufactured with fine and coarse powder mixtures [J]. Journal of Central South University, 2020, 27: 334−343.

[17] ZHANG Qiang, CHEN Jing, TAN Hua, LIN Xin, HUANG Wei-dong. Microstructure evolution and mechanical properties of laser additive manufactured Ti−5Al−2Sn−2Zr−4Mo−4Cr alloy [J]. Transactions of Nonferrous Society of China, 2016, 26: 2058−2066.

[18] KHAIRALLAH S A, ANDERSON A. Mesoscopic simulation model of selective laser melting of stainless steel powder [J]. Journal of Materials Processing Technology, 2014, 214(11): 2627−2636.

[19] GUSAROV A V, YADROITSEV I, BERTRAND P,

SMUROV I. Model of radiation and heat transfer in laser-powder interaction zone at selective laser melting [J]. Journal of Heat Transfer: Transactions of the ASME, 2009, 131: 072101.

[20] MUKHERJEE T, WEI H L, DE A, DEBROY T. Heat and fluid flow in additive manufacturing—Part I: Modeling of powder bed fusion [J]. Computational Materials Science, 2018, 150: 304−313.

[21] YIN Jie, ZHU Hai-hong, KE Lin-da, HU Pan-pan, HE Chong-wen, ZHANG Hu, ZENG Xiao-yan, A finite element model of thermal evolution in laser micro sintering [J]. The International Journal of Advanced Manufacturing Technology, 2015, 83: 1847−1859.

[22] YAN W T, LIAN Y P, YU C, KAFKA O L, LIU Z L, LIU W K, WAGNER G J. An integrated process–structure–property modeling framework for additive manufacturing [J]. Computer Methods in Applied Mechanics and Engineering, 2018, 339: 184−204.

[23] LIU Peng-wei, JI Yan-zhou, WANG Zhuo, QIU Chun-lei, ANTONYSAMY A A, CHEN Long-qing, CUI Xiang-yang, CHEN Lei. Investigation on evolution mechanisms of site-specific grain structures during metal additive manufacturing [J]. Journal of Materials Processing Technology, 2018, 257: 191−202.

[24] GE Peng, ZHANG Zhao, TAN Zhi-jun, HU Chao-ping, ZHAO Guo-zhong, GUO Xu. An integrated modeling of process−structure−property relationship in laser additive manufacturing of duplex titanium alloy [J]. International Journal of Thermal Sciences, 2019, 140: 329−343.

[25] HUANG Yan-lu, LI Jian-guo, LIANG Gong-ying, SU Jun-yi. Effect of powder feeding rate on interaction between laser beam and powder stream in laser cladding process [J]. Rare Metal Materials and Engineering, 2005, 34: 1520−1523.

[26] YANG Ru-zhen, ZOU Rui-ping, YU Ai-bing, CHOI S K. Characterization of interparticle forces in the packing of cohesive fine particles [J]. Physical Review E, 2008, 78: 031302.

[27] YAO Xin-xin, GE Peng, LI Jian-yu, WANG Yi-fei, LI Tao, LIU Wei-wei, ZHANG Zhao. Controlling the solidification process parameters of direct energy deposition additive manufacturing considering laser and powder properties [J]. Computational Materials Science, 2020, 182: 109788.

[28] PITCHAI K, BIRLA S L, SUBBIAH J, JONES D, THIPPAREDDI H. Coupled electromagnetic and heat transfer model for microwave heating in domestic ovens [J]. Journal of Food Engineering, 2012, 112: 100−111.

[29] LI He, LIN Bai-quan, YANG Wei, HONG Yi-du, WANG Zheng. A fully coupled electromagnetic−thermal−mechanical model for coalbed methane extraction with microwave heating [J]. Journal of Natural Gas Science and Engineering, 2017, 46: 830−844.

[30] PANDA B K, SAHOO S. Thermo-mechanical modeling and validation of stress field during laser powder bed fusion of $AlSi_{10}Mg$ built part [J]. Results in Physics, 2019, 12: 1372−1381.

[31] SAMANTARAY M, SAHOO S, THATOI D. Modeling of thermal and solidification behavior during laser additive manufacturing of $AlSi_{10}Mg$ alloy powders and its experimental validation [J]. Journal of Laser Applications, 2019, 31(3): 032019.

[32] ZHANG Yong-cun, KONG De-kui, LIU Shu-tian. Experimental study of forced convection heat transfer of graded metal honeycomb fabricated by additive manufacturing [J]. International Communications in Heat and Mass Transfer, 2018, 98: 67−73.

[33] ANCA A, FACHINOTTI V D, ESCOBAR-PALAFOX G, CARDONA A, Computational modelling of shaped metal deposition [J]. International Journal for Numerical Methods in Engineering, 2011, 85(1): 84−106.

[34] KRILL C, CHEN L Q. Computer simulation of 3D grain growth using a phase-field model [J]. Acta Materialia, 2002, 50(12): 3059−3075.

[35] XING Hui, DONG Xiang-lei, WU Hong-jing, HAO Guan-hua, WANG Jian-yuan, CHEN Chang-le, JIN Ke-xin. Degenerate seaweed to tilted dendrite transition and their growth dynamics in directional solidification of non-axially oriented crystals: A phase-field study [J]. Scientific Reports, 2016, 6: 26625.

[36] CHANG K, KRILL C E, DU Q, CHEN L Q. Evaluating microstructural parameters of three-dimensional grains generated by phase-field simulation or other voxel-based techniques [J]. Modelling and Simulation in Materials Science and Engineering, 2012, 20(7): 075009.

[37] ZHANG Zhao, YAO Xin-xin, GE Peng. Phase-field-model-based analysis of the effects of powder particle on porosities and densities in selective laser sintering additive manufacturing [J]. International Journal of Mechanical Sciences, 2020, 166: 105230.

[38] ZHANG Zhao, TAN Zhi-jun, YAO Xin-xin, HU Chao-ping, GE Peng, WAN Zhen-yu, LI Jian-yu, WU Qi. Numerical methods for microstructural evolutions in laser additive manufacturing [J]. Computers & Mathematics with Applications, 2019, 78(7): 2296−2307.

[39] SAHOO S, CHOU K. Phase-field simulation of microstructure evolution of Ti−6Al−4V in electron beam additive manufacturing process [J]. Additive Manufacturing, 2016, 9: 14−24.

[40] SAHOO S. An approach toward multiscale modeling of direct metal laser sintering process [J]. Metal Powder Report, 2019, 74(2): 72−76.

[41] ATAIBIS V, TAKTAK S. Characteristics and growth kinetics of plasma paste borided C_p-Ti and Ti6Al4V alloy [J]. Surface and Coatings Technology, 2015, 279: 65−71.

[42] GIL F J, PLANELL J A. Behaviour of normal grain growth kinetics in single phase titanium and titanium alloys [J]. Materials Science and Engineering A, 2020, 283: 17−24.

[43] NANDY J, YEDLA N, GUPTA P, SARANGI H, SAHOO S, Sintering of AlSi10Mg particles in direct metal laser sintering process: A molecular dynamics simulation study [J]. Materials Chemistry and Physics, 2019, 236: 121803.

[44] CRANE C A, PANTOYA M L, WEEKS B L, SAED M. The effects of particle size on microwave heating of metal and metal oxide powders [J]. Powder Technology, 2014, 256: 113−117.

[45] SHAO Jia-yun, YU Gang, HE Xiu-li, LI Shao-xia, CHEN Ru, ZHAO Yao. Grain size evolution under different cooling rate in laser additive manufacturing of superalloy [J]. Optics & Laser Technology, 2019, 119: 105662.

[46] MANVATKAR V, DE A, DEBROY T. Heat transfer and material flow during laser assisted multi-layer additive manufacturing [J]. Journal of Applied Physics, 2014, 116(12): 124905.

定向能量沉积增材制造过程中粉末对凝固影响的数值模拟

姚欣欣，李健宇，王艺飞，高 翔，张 昭

大连理工大学 运载工程与力学学部 工程力学系 工业装备结构分析国家重点实验室，大连 116024

摘 要：对激光定向能量沉积增材制造过程中粉末对颗粒温度和显微组织的影响进行模拟。利用离散元法模拟金属粉末颗粒的空间分布；借助电磁波理论分析，计算颗粒和激光的相互作用时飞行颗粒所消耗的能量。结合相场法，研究颗粒尺寸对显微组织演变的影响。通过与实验观察到的显微组织进行对比来验证模型的有效性。结果表明，窄粒度分布有利于获得更加均匀的沉积层温度，并有利于在样品侧面形成较小的等轴晶；适当尺寸的粉末颗粒有利于将电磁能转化为热能。粒径小的颗粒有助于形成等轴晶粒，提高产品质量；合适的粉末流量可以提高激光能量效率；较高的粉末流量使得截面两侧的等轴晶粒分布更加均匀。

关键词：增材制造；粉末颗粒；相场；显微组织演变；颗粒尺寸分布

(Edited by Wei-ping CHEN)